A physically-informed machine learning model for freeform bending

Philipp Lechner[1,2] · Lorenzo Scandola[3] · Daniel Maier[3] · Christoph Hartmann[3] · Yevgen Rizaiev[3] · Mona Lieb[3]

Abstract

This work aims at a fast computational process model of the free-form bending process. It proposes a novel physically-informed machine learning model, which is trained with experimental data of bending constant radii and utilizes additional physical bending knowledge by integrating Timoshenko's beam theory. The model is able to predict the resulting plastic deformation of the tube after exiting the die by computing an elastic representation of the tube's deformation with beam theory at each time step. This elastic representation serves as input for a regression model similar to a partially connected neural network. This physically-informed machine learning model generalizes the constant training radii to complex bend geometries consisting of transitional sections and true spline geometries. It is compared to a benchmark finite element simulation and has an improved prediction quality for complex kinematics while reducing the computation time by four orders of magnitude.

Introduction

Freeform bending is a kinematically-controlled bending process that can create complex 3D geometries. In addition to

Philipp Lechner and Lorenzo Scandola have contributed equally to this work.

✉ Philipp Lechner
philipp.lechner@uni-a.de

Lorenzo Scandola
lorenzo.scandola@utg.de

Daniel Maier
daniel.maier@utg.de

Christoph Hartmann
christoph.hartmann@utg.de

Yevgen Rizaiev
yevgen.rizaiev@tum.de

Mona Lieb
mona.lieb@tum.de

[1] Institute of Materials Resource Management, University of Augsburg, Am Technologiezentrum 8, 86159 Augsburg, Germany

[2] Centre for Advanced Analytics and Predictive Sciences, University of Augsburg, Universitätsstraße 2, 86159 Augsburg, Germany

[3] Technical University of Munich, Walther-Meissner-Strasse 4, 85748 Garching, Germany

arc-shaped geometries, it also allows the bending of pure 3D splines. On the other hand, this increased flexibility requires a more complex design of the bending head kinematics and a more advanced set of tools to design the bending kinematics. When predicting bending processes, a distinction is made between simulations based on the physics of the process and data-based modeling.

Physics-based process simulation

For freeform bending processes of metal tubes, the literature mainly contains simulations and analytical approaches that predict the geometry or the stress states. Simulative approaches are listed first. Maier et al. (2021) use a numerical simulation model of freeform bending with a moving die. By varying the degrees of freedom of the machine, the simulation allows the computation of geometry and residual stresses. Stebner et al. (2021) deal with the development of a soft sensor that can derive mechanical properties of a bent tube as a basis for control. Accordingly, a simulation model for the freeform bending of tubes with a moving die is developed. Based on plasticity theories, Wang and Agarwal (2006) develop analytical models to predict the cross-sectional distortion and thickness change of tubes under different loading conditions. The publication of Zhang and Wu (2016) focuses on the simulation of bending and springback processes in

tube bending. The verification of the results is done by the finite element method (FEM). A variety of approaches use the finite element method to predict the bending process. Gantner et al. (2004), deal with the finite element (FE) simulation of complex bending processes using a non-linear simulation programme. Engel and Kersten (2011) and Vatter and Plettke (2013) also take up the prediction of the bending results of the three-roll bending process using finite element methods. Hagenah et al. (2010) optimize the finite element method by adjusting deflection characteristics of the rolls. This procedure minimizes the difference between calculation and experiment. Furthermore, the simulation of tube bending is the first step in the development of a simulation model of a hydroforming process chain. For this free bending process with 6 degrees of freedom, Beulich et al. (2017) develop a finite element simulation model.

Furthermore, the prediction of bending processes using data-based approaches should be considered, since they offer short evaluation times with little computational effort compared to the numerical solving of differential equations. In addition, they can capture process effects in the experimental data that are difficult to model with a purely physical approach.

Data-based process models and hybrid approaches

Wu et al. (2022) predict the forming trajectory based on the Kalman filter algorithm. A section-by-section presentation of the motion and observation model of the tube forming, and performance of corresponding computation and analysis is given. Furthermore, Elchalakani et al. (2002) present a theoretical and experimental prediction of moment-rotation responses of circular hollow steel tubes under pure bending. Sun et al. (2022b) use a real-time prediction method improved by digital twins to bend metal tubes based on multi-source input multi-task learning.

Lou and Stelson (2001a) use a process control method for optimization that minimizes the total tube error. Measured data from the same batch are used to calculate and compensate for springback. Based on this, Lou and Stelson (2001b) present in the second part of the paper a statistical method to analyze and improve the 3-D tube bending accuracy. The relationship between the bending process error and the tube geometry error is presented using a Monte Carlo simulation. A bending correction algorithm determines the bending commands required for optimization. A publication by Zhou et al. (2021) provides a prediction of the springback angle in rotational tensile bending of round metal tubes considering the cross-sectional distortions. An extended radial basis function is introduced, which establishes a relationship between the characteristic parameters and the cross-sectional distortion. To improve the bending shape accuracy, Zhang et al. (2021) develop a springback prediction model for tubes with variable curvature. The model is based on the Frenet curve formula of the springback angle prediction of a tube with fixed curvature. Consequently, the tube curve equation is obtained, which includes the compensation amount for the springback error of the metal tube. Furthermore, Sun et al. (2022a) deal with the prediction of springback in tube bending with focus on axial accuracy. The optimization framework includes deep learning network as prediction module to predict springback more reliably. The radius change series is used here as the evaluation index for axial accuracy.

In addition, some data-based approaches for predicting sheet metal bending processes can be found in the literature. To predict the V-matrix bending process, Baseri et al. (2012) use neural network approaches with radial basis function and neural networks with error feedback. The springback is determined based on data from experimental observations. Moreover, Jafari et al. (2015) deal with the prediction of the sheet metal forming process in L-bending using artificial intelligence. First, a finite element model is combined with a Taguchi experimental design to form a design matrix. On top of this, an adaptive neuro-fuzzy inference system is applied to establish intelligent relationships between process inputs and springback.

Furthermore, Liu et al. (2021) propose a compensation method to overcome the occurring springback in sheet metal forming processes. Theory-based regularization methods are used to train deep neural networks. The learning of these networks takes place with the help of the relationship between the workpiece shape after springback and the required process parameter.

In the following, approaches are presented that use data generated by simulation to train data-based models. This offers the chance to teach the knowledge present in the simulative data to a fast-computing surrogate model. Furthermore, there is no experimental data necessary for the training, which lowers the cost of generating the full dataset. However, this method also reproduces modelling errors already present in the simulation. Kazan et al. (2009) deal with the development of a model for the prediction of springback in sheet metal bending using a neural network. Numerical simulations are performed using the finite element method to obtain teaching data for the neural network. In addition, Ma et al. (2021) develop a method for controlling springback in tube bending based on machine learning modeling. A machine learning model is used here, whereby the influences of material, geometry, and process parameters on the springback are included. Training data for the algorithm are obtained from historical production processes or alternatively from finite element simulations. Stebner et al. (2021) implement a hardness-based correlation scheme in an extended Kalman filter for the prediction of a tube bending process with a moving die. The result is a prediction of residual stresses, local strength, and strain level. Lechner et al. (2024) propose a combination of

two data-based models for a global geometry control, which provide a global optimization of the parts geometry in real-time. These data-based models are trained with simulation data.

Discussion of the research gap and objectives

The following comparative summary shows the state of the art with the advantages and disadvantages of the individual methods for predicting the bent geometry:

Physics-based process simulation

+ High accuracy
+ Flexible approach, adaptable to new boundary conditions and materials
− Computational effort of model evaluation
− Some effects challenging to model accurately

Data-based process simulation with experimental data

+ Low computational effort for evaluation of the model
+ Captures effects in experimental data which are challenging to model
− Bound to the process settings of the training data set.
− Big data sets necessary for training

Data-based process simulation with simulation data

+ Low computational effort for evaluation of the model
+ No expensive experimental data necessary
− Bound to the process settings of the training data set.
− Big data sets necessary for training
− Accuracy limited by the accuracy of the simulation

This article attempts to combine the advantages of physical modeling and the usage of a data-based model trained with experimental data. A physics-informed machine learning model that integrates physical process knowledge into the training, but is trained on experimental data, offers the chance to have a low computational effort combined with a reduced need for experimental data, since basic physics is introduced with equations into the model. Additionally, the model can learn effects which are challenging to model (e.g. friction) from experimental data. This aims at creating a very fast computational surrogate model with a small data set and low experimental effort, suitable for inverse analysis and real-time process control, and with the predictive accuracy of an FEM simulation.
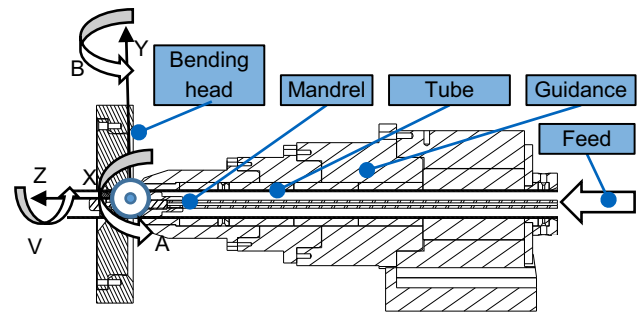

Fig. 1 Freeform bending system with movable bending head used for the experiments

Table 1 Chemical composition of the utilized specimens in %

C	Si	Mn	P	S
< 0.16	< 0.35	< 1.20	< 0.025	< 0.020
Cr	Cu	Mo	Ni	V
< 0.30	< 0.30	< 0.08	< 0.30	< 0.02

Materials and methods

Bending setup and material

Figure 1 shows a schematic of the Jörg Neu GmbH bending machine used for this article. It has three translational and three rotational degrees of freedom. The tube is pushed by the feed Z through a guidance and bent by a bending head that can be rotated around three axes (degrees of freedom A, B, V) and moved translationally in the x and y directions (degrees of freedom X and Y). Since only round tubes are considered in this article, rotation V is neglected. Bending takes place in the free bending length between the bending head and the guide. Inside the tube, a mandrel composed of movable links is placed in the free bending length, which delays tube stability problems such as buckling.

In this article, steel (P235TR1) tubes with 33.7 mm diameter and 2 mm wall thickness are used. The tubes were mechanically characterized by Stebner et al. (2021) which is the basis for the material model in this article. The chemical composition of the specimens is shown in Table 1.

Training and validation geometries

Different geometries are used to train and validate the process models. The physics-based machine learning model is trained with 75 constant radii that are bent and optically measured. The optical measurement system used for the geometry acquisition is composed by the handheld scanner T-Scan and the measuring bar T-Track 10 by Zeiss, which ensures an accuracy of 0.33 mm + 0.33 mm/m and provides a measurement volume of 10mm^3. In the simulation, various
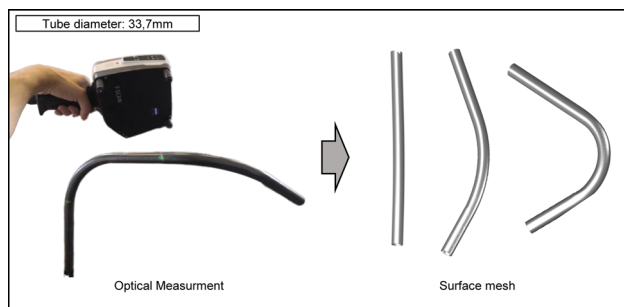
Fig. 2 Measurement with the Zeiss T-Scan and exemplary results with a constant radius, which are utilized for the training of the models

numerical parameters are adjusted to best represent these 75 measured radii as well. The bending head is moved with a constant rotation and translation to achieve these radii. Each time a 100 mm tube segment is bent. The specimens are optically measured with the Zeiss T-Scan measuring device, which results in a triangulated surface mesh of the specimen. Figure 2 shows three example surface meshes with varying constant radii. To evaluate the data, an arc is fitted in the area of the tube with constant radius, while the parts of the tube which are produced with a moving die are neglected to achieve a clear correlation between position and orientation of the bending head and resulting curvature of the tube. The full data set is presented in the appendix in Tables 4 and 5. In addition, the degrees of freedom (DOFs) on the horizontal and vertical planes are symmetric. This allows the dimension of the data to be reduced, without losing accuracy. The bending of the 75 radii covers one quadrant of the bending heads workspace. Due to the inherent symmetries of the process, the results can be transferred to the other three quadrants, increasing the total data set to 300 data points. In order to perform a representative choice of the experimental data points for the training, the domain of the DOFs has been investigated. On a bending plane, always two DOFs are active, namely one translation and one rotation. These are independent, and can be related to each other using their ratio $r = \text{translation/rotation}$. Since in free-form bending the obtained radius correlates quadratically with the translation, it is practical to define as input quantities a set of translations and a set of radii. For this reason, Tables 4 and 5 show recurring values of the translation with different rotations. The translations have been chosen in the range 2-18 mm in steps of 2 mm, in order to cover the range of mild (< 9 mm), moderate (11–15 mm) and severe (> 15 mm). The ratios have been chosen in the range 0.15–2.5, in steps of 0.1 until $r = 1$ and 0.2 from $r = 1.2$, in order to ensure that forming by overbending ($r < 1$) as well as underbending ($r > 1$) is represented in the training data set. Finally, the presented investigations concern a single material, and are aimed at showing the suitability of the implemented method for predicting the final

geometry of the components. The implemented framework would still deliver meaningful results by changing the material. Nevertheless, a new training with the new material would be required.

The accuracy of the simulation and the physics-based machine learning model are tested with validation geometries shown in Fig. 3. For each geometry, the optical measurement after bending and the corresponding bending head kinematics are shown. Geometries 1, 2 and 4 are classic bending geometries with constant rotation-translation segments, while geometry 3 is a true spline geometry that uses the full capabilities of the free-form bending machine. Validation is a two-step process. Geometries 1 and 2 are used with the full parameter set, while geometries 3 and 4 are used for validation after reducing the model complexity based on the results of evaluating geometries 1 and 2. Within these geometries the transitional sections between constant segments need special focus, since they have a significant influence on the resulting geometry of the part and they cannot be interpolated from experiments with constant rotation-translation settings, due to the moving bending head in these segments. Therefore, true spline geometries like geometry 3 are very challenging to model, since the bending head is moving most of the time during production. These segments are well suited to test the generalization capabilities of the models.

Finite element simulation

The finite element simulation is built in Abaqus and is shown in Fig. 4. The tube is meshed with S4R shell elements (20-40 elements around the pipe circumference). The bending head, the mandrel and the guidance are meshed with R3D4 elements. The flow curves published by Stebner et al. are utilized in the material model (Stebner et al., 2021). The Young's modulus is chosen to 210 GPa, the Poisson ratio to 0.3. Due to tolerances of the tools and the tubes, the maximum possible clearance between tool and tube is 0.7 mm, which is implemented in the simulation. The kinematics of the bending process is implemented in the constraints of the feed and bending head for all degrees of freedom (A, B, X, Y, Z) of the process. The simulation serves as a benchmark for the accuracy of the physics-informed machine learning model. To make this benchmark as challenging as possible, the simulation is fit to the same training data as the machine learning model, optimizing the friction coefficient, the mesh size and the mass scaling in the process to minimize the error of the simulation compared to the experimental data. In a full-factorial simulation study, the friction coefficient is set to [0.01, 0.025, 0.05], the number of nodes on the circumference of the tube to [20, 30, 40], and the mass scaling to [500, 1200, 2000, 5000, 7500, 10000]. The full-factorial study results in 4050 simulations, which serve as support points in a grid search for the best simulation parameters
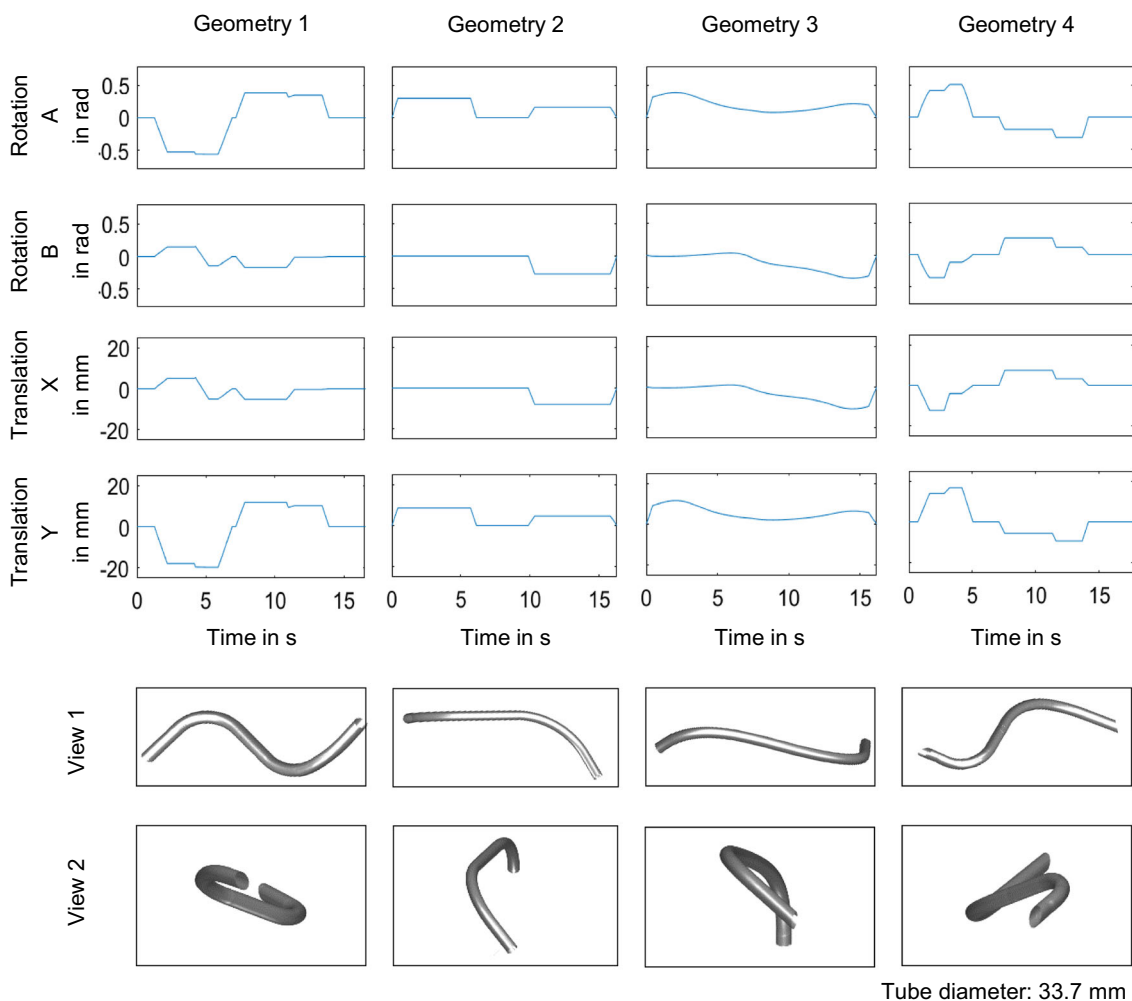
Fig. 3 Validation geometries used in this article. Geometries 1, 2 and 4 are classical bending geometries with constant rotation-translation segments, while geometry 3 is a true spline geometry

by minimizing the absolute error of the predicted curvature compared to the 75 experimental specimens. A comparison for the best parameter set with a friction coefficient of 0.01, a mass scaling of 5000 and 20 nodes distributed over the tube circumference is shown in Fig. 5. Figures 13, 14 and 15 in the appendix show further exemplary results of this parameter study.

Physically-informed machine learning model

The physically-informed machine learning model (PIMLM) has two main interlocking components. A data-based model that calculates six correction parameters and an analytical beam model that introduces engineering knowledge about the process. The analytical beam model uses Timoshenko's beam theory to calculate artificial purely elastic deflections w of the tube between the guidance and the bending head. The influence of plasticity on w is not considered in this evaluation due to the computational complexity of a solution with
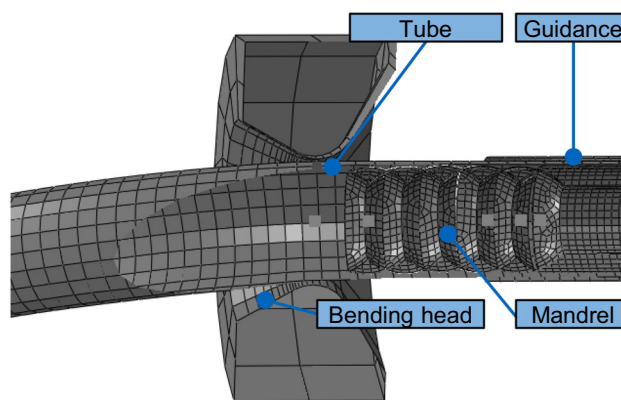

Fig. 4 Explicit finite element simulation of the bending process

an elastic and a plastic part in the deformation. These elastic calculations do not result in the real deformation of the tube,
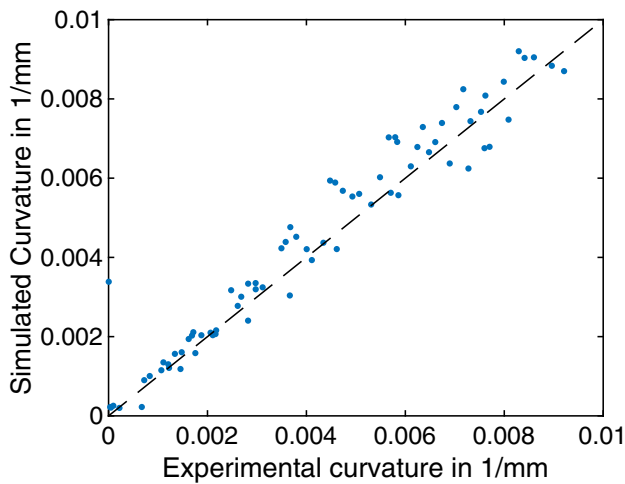
Fig. 5 Comparison between the experimentally obtained curvatures and the simulated ones for a friction coefficient of 0.01, a mass scaling of 5000 and 20 nodes distributed over the tube circumference

but serve as input to the following machine learning model, which in turn maps them to plastic deformations of the tube based on the experimental training data. Thus, the subsequent data-based model component is trained to compensate for this simplification. This allows to replace the computationally expensive calculation of the plastic deformation, which will still contain inaccuracies with a fast-calculating data-based approach.

Therefore, the fast beam theory for elastic deflections will be utilized:

$$\frac{dw(z)}{dz} = \frac{dw_B(z)}{dz} + \frac{dw_S(z)}{dz}, \tag{1}$$

$$w(z) = w_B(z) + dw_S(z), \tag{2}$$

where w_B is the deflection due to bending and w_S the deflection due to shear. This leads to the following differential equations:

$$\frac{d^2 w_B(z)}{dz^2} = \frac{C_1}{EI}z + \frac{C_2}{EI}, \tag{3}$$

$$\frac{dw_B(z)}{dz} = \frac{C_1}{2EI}z^2 + \frac{C_2}{EI}z + \frac{C_3}{EI}, \tag{4}$$

$$\frac{dw_S(z)}{dz} = -\frac{C_1}{GA_s}, \tag{5}$$

which leads to:

$$w(z) = \frac{C_1}{6EI}z^3 + \frac{C_2}{2EI}z^2 + \frac{C_3}{EI}z + \frac{C_4}{EI} - \frac{C_1}{GA_s}z + C_5, \tag{6}$$

where C_1-C_5 are integrational constants, E is the Young's Modulus and G the shear modulus.

Figure 6 (left) shows a schematic of the mechanical setup with the reference coordinate system. The boundary conditions of the differential equations are as follows:

$$w(0) = 0, \ w_S(0) = 0, \ w(l) = X, \tag{7}$$

$$\frac{dw_B}{dz}(0) = 0, \ \frac{dw_B}{dz}(l) = \tan B, \tag{8}$$

where B is the rotation around the y-axis and X the translation of the bending head. This calculation is performed analogously for translations of the bending head in y-direction and rotations around the x-axis.

The arc length is discretized into bending segments and the bending history of each discrete segment is used to calculate the plastic deformation of that bend step. Figure 6 (right) shows an example bending history of the segment marked with the red dot just leaving the bending head. The bending line is calculated by superposition.

The hypothesis is that for each discrete bending segment, there is an interval of interest with amplitudes of the bending kinematics A, B, X, and Y that occurred when the bending section was at the free bending length l between the bending head and the guide. These amplitudes within the interval of interest determine the plastic deformation of the tube. This means that for each degree of freedom of the machine, several past amplitude values in the interval of interest affect the plastic deformation of the current discrete bending section. The number depends on the step size of the discretization and the free bending length.

In this article, a discretization of 1 mm has been chosen. Preliminary studies have shown, that this is a robust compromise between calculation time and accuracy. This means that for the given free bending length of 42 mm, 42 values for each degree of freedom are used in the computation of the plastic deformation and build the interval of interest for the respective bending segment. The plastic deformation is simplified and assumed to be ideally plastic with no elastic component. This reduces the necessary computational effort, while this simplification is later corrected by the data-based model. Thus, the plastic deformation is calculated by integrating the bending history. The plastic deformation is calculated in spherical coordinates. The step size results in the respective sphere radius, while the plastic deformation is described by two angles α and β, as visualized in Fig. 6. By adding these discrete bending segments, the resulting arc line can be calculated. The generation of the arc line is done iteratively for all n tube segments. Each segment i ends with a point P_i. The vector v_i between two points is calculated in cylindrical coordinates with α, β and the discretization step length as arc length. The absolute coordinates of the end point of segment i are calculated by summing all previous vectors $v_1 - v_i$ in Cartesian coordinates. This is visualized in Fig. 6.

Fig. 6 Discretization of the bending history of each bending segment. The points P describe the arc line of the geometry with the vectors $v_{i+1} = P_{i+1} - P_i$
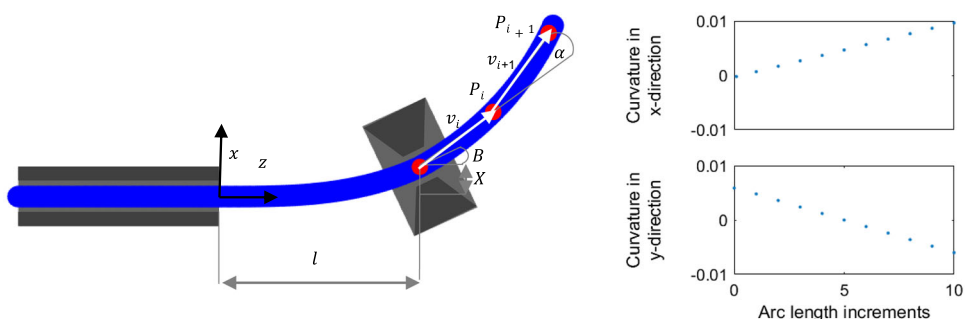
This simplified analytical model for the plastic deformation of the tube described above is corrected by the data-based model with six correction parameters. The resulting α and β angles are multiplied by R_x and R_y to correct the plastic deformation. Furthermore, there are offsets for the kinematic boundary conditions, since the beam model assumes an ideal contact. In reality, however, there is a difficult-to-predict air gap between the tube and the tools of the machine, which is necessary to be able to insert the tube and to account for the manufacturing tolerances of the semi-finished product. Therefore, the degrees of freedom A, B, X, Y can be corrected, resulting in adjusted boundary conditions for the beam model:

$$w_x(0) = 0, \quad \frac{dw_{Bx}}{dz}(0) = 0, \tag{9}$$

$$w_x(l) = X + \Delta X, \quad \frac{dw_{Bx}}{dz}(l) = \tan(B + \Delta B), \tag{10}$$

$$w_y(0) = 0, \quad \frac{dw_{By}}{dz}(0) = 0, \tag{11}$$

$$w_y(l) = Y + \Delta Y, \quad \frac{dw_{By}}{dz}(l) = \tan(A + \Delta A), \tag{12}$$

These correction parameters are calculated by the data-based model using four input values, each calculated from the maximum absolute amplitude values in the interval of interest affecting the respective bending segment.

The data-based model is created using a regression model in Matlab, which basically works like a single layer feedforward neural network using linear transfer functions. The correction parameters are computed as follows:

$$\begin{aligned} \Delta B = &\ p_1(p_2 B_{max,abs} + p_3 X_{max,abs} + p_4) \\ &+ p_5(p_6 * B_{max,abs} + p_7) \\ &+ p_8(p_9 * X_{max,abs} + p_{10}) + p_{11} \end{aligned} \tag{13}$$

$$\begin{aligned} \Delta X = &\ p_{12}(p_{13} B_{max,abs} + p_{14} X_{max,abs} + p_{15}) \\ &+ p_{16}(p_{17} * B_{max,abs} + p_{18}) \\ &+ p_{19}(p_{20} * X_{max,abs} + p_{21}) + p_{22} \end{aligned} \tag{14}$$

$$\begin{aligned} R_x = &\ p_{23}(p_{24} B_{max,abs} + p_{25} X_{max,abs} + p_{26}) \\ &+ p_{27}(p_{28} * B_{max,abs} + p_{29}) \end{aligned}$$

$$+ p_{30}(p_{31} * X_{max,abs} + p_{32}) + p_{33}, \tag{15}$$

where $p_1 - p_{33}$ represent the model parameters, which are adjusted using a quasi-Newtonian algorithm to minimize the loss function of the entire model. $B_{max,abs}$ and $X_{max,abs}$ are scalar values calculated as the maximum of the absolute magnitude of the respective amplitudes of the degrees of freedom in the interval of interest that determined the bending histories.

In the loss function of the optimization, the mean error of the prediction of the angles α and β compared to the experimental data is calculated. The parameters ΔA, ΔY and R_y are calculated and optimized analogously as a function of $A_{max,abs}$ and $Y_{max,abs}$. This leads to a total number of 66 parameters for the data-based model. The optimization of the vector $\boldsymbol{p}$ containing all parameters $p_1 - p_{66}$ with n data-points in the training data follows Expression 16:

$$\arg\min_{\boldsymbol{p}} \left\{ \sqrt{\sum_{i=1}^{n} \begin{bmatrix} \alpha_i^{exp} - \alpha_i^{ml} \\ \beta_i^{exp} - \beta_i^{ml} \end{bmatrix}^2} \right\}, \tag{16}$$

where α_i^{exp} and β_i^{exp} are experimentally obtained values of data point i and α_i^{ml} and β_i^{ml} are the results of the model evaluation. The data set was split into training and testing data with 15% of the data set being reserved for testing purposes to avoid overfitting. Engineering considerations are already incorporated, such as the symmetry between x and y directions and the superposition principle between these two spatial directions in beam theory. Furthermore, the connections are chosen such, that each output is calculated with three summands: One for each of the two possible inputs and one for a linear combination of the two inputs. The reasoning is that each of the summands may be necessary to find an accurate solution. The importance of the summand for the solution can be found in the value of the respective parameters. Therefore, it will be possible to reduce the model complexity, by taking out the smallest summands in an optimization ("Reduction of model complexity" section). In contrast to a fully connected neural network, this data-based model has fewer free parameters and can thus be trained with fewer data points with a low risk of overfitting. Thus,

Fig. 7 Architecture of the physically-informed machine learning model
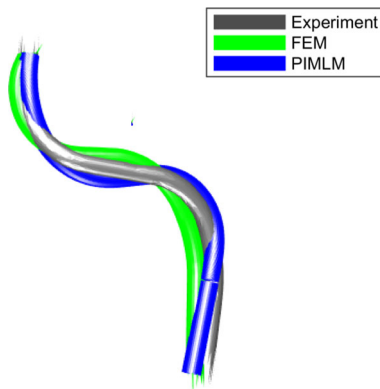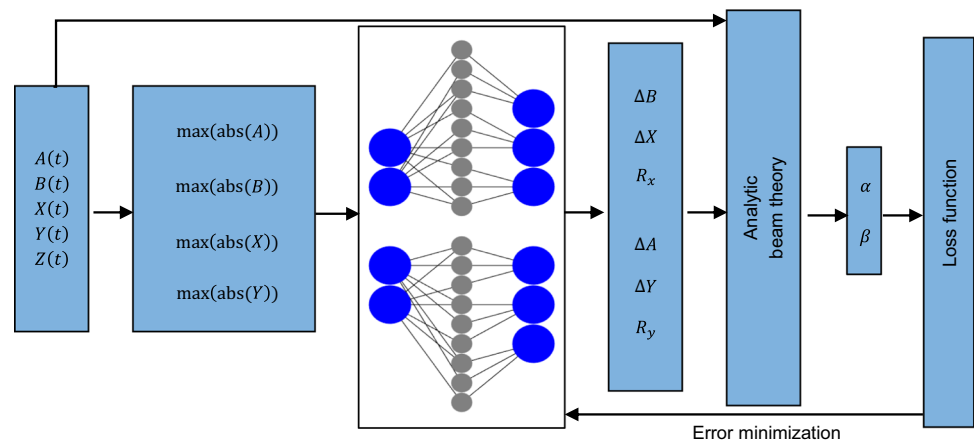

Fig. 8 Results from the finite element model (green) and the physically-informed machine learning model (blue) fitted to the experimental data (gray) of geometry 1 (Color figure online)
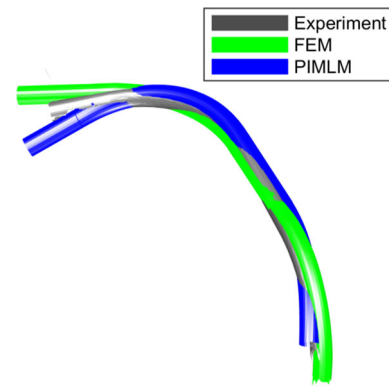
Fig. 9 Results from the finite element model (green) and the physically-informed machine learning model (blue) fitted to the experimental data (gray) of geometry 3 (Color figure online)

the physics-informed character of the model is further developed and a physics-informed architecture of the data-based model is designed. The architecture and training of the whole model is shown in Fig. 7.

Comparison between the full physically-informed machine learning model and the finite element computation

In the following, the results of the geometry computations performed with the full physically-informed machine learning model, the results of the finite element computation and the experiments are compared for the validation geometries 1-4. Figures 8 and 9 show the global best fits of the two models to the optical measurement of the experimental part for geometries 1 and 3 as an example. For both modeling approaches, geometric errors remain compared to the experiments. A part of the errors in the modeling can be attributed to the material model, which does not account for variations in the material of the tubes from batch to batch. Furthermore, the dimensions of the tubes are varying, which we

did not take into account. In addition, process friction is known to have an effect on the resulting geometry, which is difficult to model accurately in finite element simulations. The data-based approach offers the opportunity to learn from experiments, but it is similarly susceptible to geometric tolerances and material fluctuations. Furthermore, the friction coefficients for complex geometries with a moving bending head may differ from the components with constant radius in the training data set.

The root mean square error (RMSE) of the iterative closest point algorithm used for the fit can be interpreted as a global error measure. Table 2 shows the errors of the two models and their computation times. The PIMLM leads to a reduction of the global geometry error for geometries 1 and 2, while it has a similar prediction quality for geometry 3 and an increased error for geometry 4. Overall, the average error of all four validation geometries is improved. However, the most important finding is that it reduces the computation time by four orders of magnitude to less than one second combined with an improved accuracy in three out of four test cases.

Table 2 Comparison of finite element model and physically-informed machine learning model computations for geometries 1–4

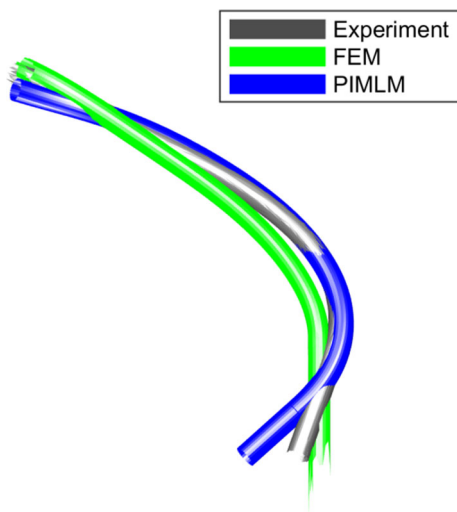|	PIMLM RMSE in mm	FE RMSE in mm	PIMLM time in s	FE time in s
Geo. 1	11.8	15.5	0.44	$6.6 * 10^3$
Geo. 2	11.7	17.9	0.45	$7.1 * 10^3$
Geo. 3	10.8	11.0	0.53	$5.4 * 10^3$
Geo. 4	7.55	5.3	0.50	$5.7 * 10^3$
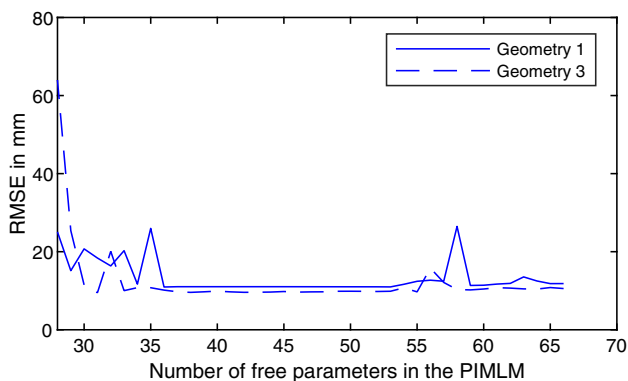
Fig. 10 Model error for two exemplary geometries and a reduction of model complexity

Fig. 11 Results from the finite element model (green) and the physically-informed machine learning model (blue) fitted to the experimental data (gray) of geometry 2 (Color figure online)
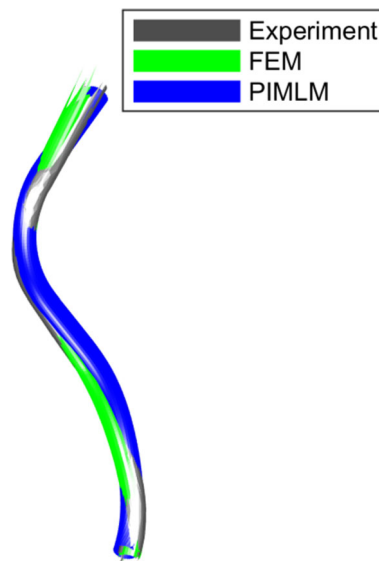

Fig. 12 Results from the finite element model (green) and the physically-informed machine learning model (blue) fitted to the experimental data (gray) of geometry 4 (Color figure online)

Reduction of model complexity

The following study analyzes the necessary complexity of the model. The previous number of parameters was chosen by a conservative evaluation, whether a relevant influence of each parameter is possible. Now the model complexity of the PIMLM is reduced by repeated training to deactivate unnecessary parameters. In each training cycle, the smallest of the parameters p_1-p_{66} is considered the least important and is set to zero. In this way, the number of parameters in the model is reduced by one at each iteration. The RMSE of validation geometries 1 and 3 for this model reduction are shown in Fig. 10. An increase in the RMSE of both geometries can be observed below 36 parameters. Therefore, a reduced model with 36 parameters is used for the final comparison between the experiment, the physically-informed machine learning model, and the finite element simulation. The repeated training of the model and the reduction of the model complexity could lead to a kind of adaptation to the validation geometries used for the reduction (geometry 1 and 3). Therefore, geometry 2 and 4 serve as independent validation geometries for the final performance test. Figures 11 and 12 show the comparison of the two models with the experimental data. Figs. 16, 17, 18 and 19 in Appendix show the individual results for α and β for future reproducibility.

Interestingly, the reduced physically-informed machine learning model has improved geometrical errors for all geometries compared to the full machine learning model, which is shown by the error measures in Table 3. This can be explained as the optimization of the model parameters is focused only on relevant parameters and the information of the limited training data set is used to train less parameters

Table 3 Comparison of the full and the reduced physically-informed machine learning model

	Full PIMLM RMSE in mm	Red. PIMLM RMSE in mm	FE RMSE in mm
Geo. 1	11.8	11.0	15.5
Geo. 2	11.7	9.63	17.9
Geo. 3	10.8	9.58	11.0
Geo. 4	7.55	6.60	5.3

with the same amount of training data, which results in a better fit to the physics of the process.

Discussion of possible applications

The physically-informed machine learning model shows better prediction quality for the validation components' geometry as a finite element simulation of the freeform bending process, which has been optimized through intensive parameter studies on the same training data set. This shows that the combination of Timoshenko's beam theory and an experimental data set is capable of better geometry prediction than a finite element formulation with much more advanced mechanical modeling for complex geometries. The mechanical knowledge brought to the data-based model by Timoshenko's beam theory allows the model, trained by constant radii, to perform well for generalized complex kinematics. The main advantage of the data-based approach is the reduced computation time combined with a high prediction accuracy, compared to a FE calculation. Of four validation geometries the physically-informed machine learning model performs better than the FE calculation in three cases (Tables 2 and 3), while reducing the calculation time by four orders of magnitude. This allows new applications of the process model. In a first step, it will be possible to compute kinematics for complex spline geometries by inversely optimizing the kinematics with an optimization algorithm. This was previously not possible due to the long computation time of the finite element model. In a second step, a fast computational model can be used for inline process control of the bending process to adapt the bending kinematics to material and batch variations in real time. Such a global process control is proposed by Lechner et al. (2024) with a purely data-based approach without additional physical knowledge.

Conclusion and outlook

In this article, a novel physically-informed machine learning model is proposed to predict part geometry based on the kinematics of a freeform bending process. The data-

based part of the model is trained with experimental data of bending constant radii. The Timoshenko's beam theory provides additional physical knowledge to the model. Compared to a benchmark finite element simulation, the physically-informed machine learning model has a better prediction quality while reducing the computation time by four orders of magnitude. As a result, this process model can be used for inverse kinematics optimization in the future. In future research, we will study the generalizability of the physically-informed machine learning model to give indications when to use it. Furthermore, we will analyze how the prediction quality is dependent on the complexity of the model and the amount of training data. A future investigation will also involve the generation of a meta-model from multiple materials which enables geometry prediction for a broad range of materials.

Appendix

Table 4 Training data of constant radii

Translation in mm	Rotation in deg	Radius (mm)
2	13.33	1488.25
2	6.67	4544.78
4	13.33	687.64
6	20	354.59
4	10	817.87
5	12.5	570.03
6	15	459.76
8	20	272.9
2	4	10376.32
4	8	937.24
6	12	462.53
8	16	299545
10	20	216.77
12	24	170.67
14	28	137.45
6	10.91	474.7
12	21.82	175.29
15	27.27	129.84
5	8.33	676.65
6	10	485
8	13.33	321.05
10	16.67	230.25
12	20	182.24
14	23.33	145

Table 4 continued

Translation in mm	Rotation in deg	Radius (mm)
15	25	131.59
16	26.67	123.67
18	30	108.6
8	11.43	336.39
10	14.29	243.35
12	17.14	188.37
14	20	154.38
15	21.43	136.69
16	22.86	131.27
18	25.71	111.6
2	2.5	20961.82
4	5	1201.7
5	6.25	745.88

The translation and the rotation refers to the kinematics of the bending head, while the radius describes the resulting constant radius of the bent tube

Table 5 Training data of constant radii—Part 2

Translation in mm	Rotation in deg	Radius (mm)
6	7.5	533
8	10	336.2
10	12.5	249.69
12	15	197.4
14	17.5	160.18
15	18.75	148.37
16	20	132.82
18	22.5	116.29
15	16.67	151.41
18	20	118.91
6	6	583.62
8	8	354.42
10	10	263.58
12	12	202.88
14	14	163.65
16	16	139.45
18	18	120.6
2	1.67	30155.94
4	3.33	1387.42
5	4.17	828.5
6	5	593.02
8	6.67	372.86
10	8.33	286.16
12	10	211.18
14	11.67	171.38

Table 5 continued

Translation in mm	Rotation in deg	Radius (mm)
15	12.5	157.41
16	13.33	142.25
18	15	125.17
8	5.71	382.99
10	7.14	279.33
12	8.57	218.27
14	10	172.57
6	3.75	617.42
8	5	403.52
10	6.25	272.18
12	7.5	223.32
14	8.75	176.56
5	2.63	901.83
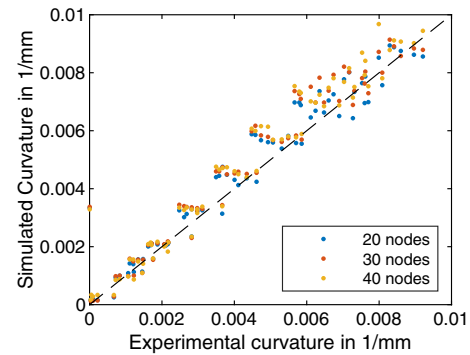
Fig. 13 Comparison of experimental and finite element results with a variation of the number of nodes distributed of the circumference of the tube with a friction coefficient of 0.01 and a massscaling of 500
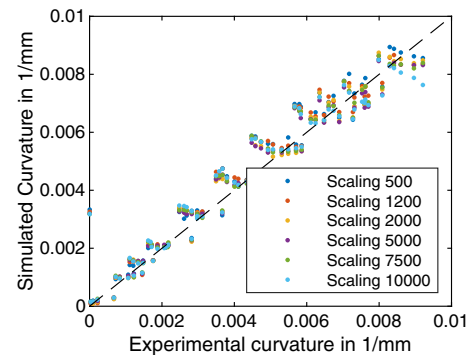
Fig. 14 Comparison of experimental and finite element results with a variation of the implemented massscaling with a friction coefficient of 0.01 and 20 nodes distributed over the circumference of the tube
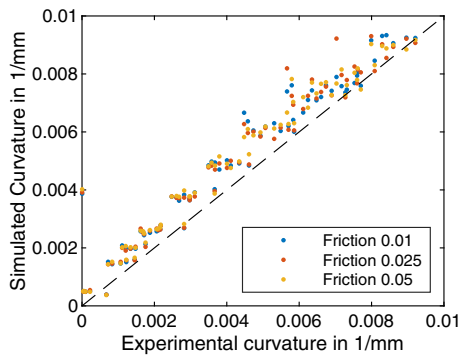
Fig. 15 Comparison of experimental and finite element results with a variation of the friction coefficient with a massscaling of 500 and 20 nodes distributed over the circumference of the tube
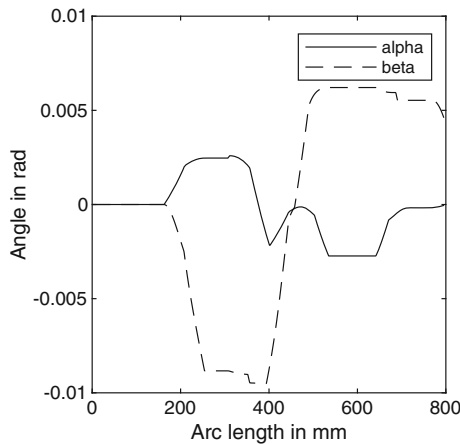

Fig. 16 Bending angles describing the curvature of geometry 1, calculated with the PIMLM in "Reduction of model complexity" section
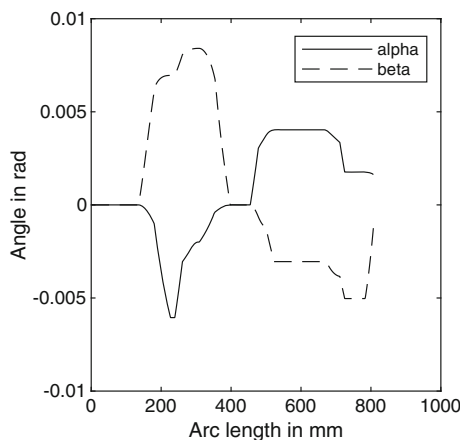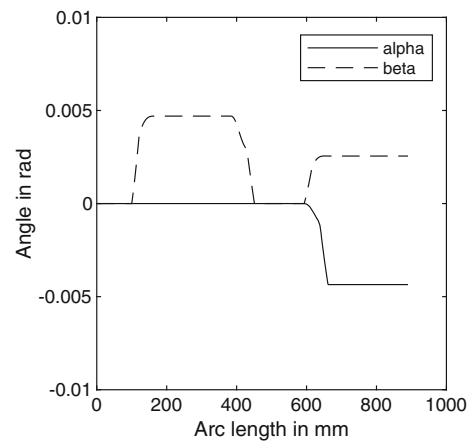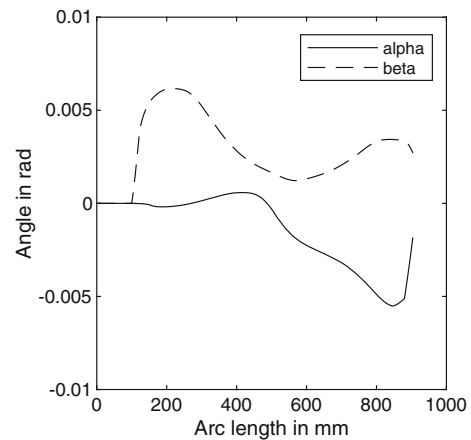

Fig. 17 Bending angles describing the curvature of geometry 2, calculated with the PIMLM in "Reduction of model complexity" section

Fig. 18 Bending angles describing the curvature of geometry 3, calculated with the PIMLM in "Reduction of model complexity" section

Fig. 19 Bending angles describing the curvature of geometry 4, calculated with the PIMLM in "Reduction of model complexity" section

Declarations

Conflict of interest The authors have no relevant financial or nonfinancial interests to disclose.

References

Baseri, H., Rahmani, B., & Bakhshi-Jooybari, M. (2012). Predictive models of the spring-back in the bending process. *Applied Artificial Intelligence, 26*(9), 862–877. https://doi.org/10.1080/08839514.2012.726155

Beulich, N., Craighero, P., & Volk, W. (2017). FEA simulation of free-bending–a preforming step in the hydroforming process chain. *Journal of Physics: Conference Series, 896*(012), 063. https://doi.org/10.1088/1742-6596/896/1/012063

Elchalakani, M., Zhao, X. L., & Grzebieta, R. H. (2002). Plastic mechanism analysis of circular tubes under pure bending. *International Journal of Mechanical Sciences, 44*(6), 1117–1143. https://doi.org/10.1016/S0020-7403(02)00017-6

Engel, B., & Kersten, S. (2011) Analytical models to improve the three-roll-pushbending process of tube-profiles. In *Proceedings of the international conference on technology of plasticity. ICTP*, Aachen (pp. 355–360). https://www.tib.eu/de/suchen/id/BLCP%3ACN080660878

Gantner, P., Bauer, H., Harrison, D. K., & De Silva, A. K. M. (2004) FEA—simulation of bending process with LS-DYNA. In *8th International LS-DYNA users conference*. https://www.dynalook.com/conferences/international-conf-2004/02-5.pdf

Hagenah, H., Vipave, D., Plettke, R., & Merklein, M. (2010) Numerical model of tube freeform bending by three-roll-push-bending. In *2nd International conference on engineering optimization*. http://www1.dem.ist.utl.pt/engopt2010/Book_and_CD/Papers_CD_Final_Version/pdf/06/01506-01.pdf

Jafari, M., Lotfi, M., Ghaseminejad, P., & Roodi, M. (2015). Numerical control and optimization of Springback in L-bending of magnesium alloy through Fe analysis and artificial intelligence. *Transactions of the Indian Institute of Metals, 68*(5), 969–979. https://doi.org/10.1007/s12666-015-0535-7

Kazan, R., Fırat, M., & Tiryaki, A. E. (2009). Prediction of springback in wipe-bending process of sheet metal using neural network. *Materials & Design, 30*(2), 418–423. https://doi.org/10.1016/j.matdes.2008.05.033

Lechner, P., Scandola, L., Maier, D., & Hartmann, C. (2024) Data-based global control of the part's geometry during free-form bending. In K. Mocellin, P. O. Bouchard, R. Bigot et al. (Eds.), *Proceedings of the 14th international conference on the technology of plasticity—current trends in the technology of plasticity* (pp. 36–47). Springer. https://doi.org/10.1007/978-3-031-42093-1_4

Liu, S., Xia, Y., Shi, Z., Yu, H., Li, Z., & Lin, J. (2021). Deep learning in sheet metal bending with a novel theory-guided deep neural network. *IEEE/CAA Journal of Automatica Sinica, 8*(3), 565–581. https://doi.org/10.1109/JAS.2021.1003871

Lou, H., & Stelson, K. A. (2001a). Three-dimensional tube geometry control for rotary draw tube bending, part 1: Bend angle and over-all tube geometry control. *Journal of Manufacturing Science and Engineering, 123*(2), 258–265. https://doi.org/10.1115/1.1351813

Lou, H., & Stelson, K. A. (2001b). Three-dimensional tube geometry control for rotary draw tube bending, part 2: Statistical tube tolerance analysis and adaptive bend correction. *Journal of Manufacturing Science and Engineering, 123*(2), 266–271. https://doi.org/10.1115/1.1351812

Ma, J., Li, H., Chen, G. Y., Welo, T., & Li, G. J. (2021). Machine learning (ML)-based prediction and compensation of springback for tube bending. In G. Daehn, J. Cao, & B. Kinsey et al. (Eds.), *Forming the future* (pp 167–178). Springer. https://doi.org/10.1007/978-3-030-75381-8_13

Maier, D., Stebner, S., Ismail, A., Dölz, M., Lohmann, B., Münstermann, S., & Volk, W. (2021). The influence of freeform bending process parameters on residual stresses for steel tubes. *Advances in Industrial and Manufacturing Engineering, 2*(100), 047. https://doi.org/10.1016/j.aime.2021.100047

Stebner, S. C., Maier, D., Ismail, A., Balyan, S., Dölz, M., Lohmann, B., Volk, W., & Münstermann, S. (2021). A system identification and implementation of a soft sensor for freeform bending. *Materials (Basel, Switzerland), 14*(16), 4549. https://doi.org/10.3390/ma14164549

Sun, C., Wang, Z., Zhang, S., Liu, X., Wang, L., & Tan, J. (2022a). Toward axial accuracy prediction and optimization of metal tube bending forming: A novel GRU-integrated PB-NSGA-III optimization framework. *Engineering Applications of Artificial Intelligence, 114*(105), 193. https://doi.org/10.1016/j.engappai.2022.105193

Sun, C., Wang, Z., Zhang, S., Zhou, T., Li, J., & Tan, J. (2022b). Digital-twin-enhanced metal tube bending forming real-time prediction method based on multi-source-input MTL. *Structural and Multidisciplinary Optimization*. https://doi.org/10.1007/s00158-022-03372-0

Vatter, P. H., & Plettke, R. (2013). Process model for the design of bent 3-dimensional free-form geometries for the three-roll-push-bending process. *Procedia CIRP, 7*, 240–245. https://doi.org/10.1016/j.procir.2013.05.041

Wang, J., & Agarwal, R. (2006). Tube bending under axial force and internal pressure. *Journal of Manufacturing Science and Engineering, 128*(2), 598–605. https://doi.org/10.1115/1.2112987

Wu, J., Liang, B., & Yang, J. (2022). Trajectory prediction of three-dimensional forming tube based on Kalman filter. *The International Journal of Advanced Manufacturing Technology, 121*(7–8), 5235–5254. https://doi.org/10.1007/s00170-022-09521-5

Zhang, S., Fu, M., Wang, Z., Fang, D., Lin, W., & Zhou, H. (2021). Springback prediction model and its compensation method for the variable curvature metal tube bending forming. *The International Journal of Advanced Manufacturing Technology, 112*(11–12), 3151–3165. https://doi.org/10.1007/s00170-020-06506-0

Zhang, S., & Wu, J. (2016). Springback prediction of three-dimensional variable curvature tube bending. *Advances in Mechanical Engineering, 8*(3), 16878140166732. https://doi.org/10.1177/1687814016637327

Zhou, H., Zhang, S., Qiu, L., & Wang, Z. (2021). Springback angle prediction of circular metal tube considering the interference of cross-sectional distortion in mandrel-less rotary draw bending. *Science Progress, 104*(1), 36850420984303. https://doi.org/10.1177/0036850420984303